Research paper

# Nature-inspired interlaced printing strategies for additive manufacturing highly improved mechanical properties

Wenpeng Xu [a,1], Hao Xu [b,1], Xiaoya Zhai [c], Jingchao Jiang [d,*]

[a] *School of Computer Science Technology, Henan Polytechnic University, Jiaozuo, 454003, China*
[b] *School of Computer Science and Technology, Shandong University, Qingdao, 266237, China*
[c] *School of Mathematical Sciences, University of Science and Technology of China, Hefei, 230026, China*
[d] *Department of Engineering, University of Exeter, Exeter, EX4 4QF, UK*

## ARTICLE INFO

## ABSTRACT

In conventional additive manufacturing, the layer-by-layer approach leads to mechanical weaknesses, particularly in the vertical tensile strength (Z-axis) and the shear resistance between layers. The unique mechanism of mechanical enhancement found in natural materials has served as inspiration for solving the above problems. Here this study introduces two novel Interlaced Printing strategies for 3-axis printers inspired by nature. The proposed strategies involve moving the deposition head in the XY plane while periodically adjusting its height in the Z-axis, enhancing interlayer bonding and shear resistance. These strategies were closely examined to understand their impact on toolpath width and layer thickness, considering various parameters. Both strategies resulted in "dumbbell"-shaped toolpath geometries, a characteristic that can be lessened by reducing print speed. Mechanical tests revealed that objects printed using these strategies significantly outperform traditional planar toolpath methods in terms of mechanical strength, showing improvements of 31.9% and 67.5% in interlayer shear resistance. Notably, these new strategies can be combined with each other or with conventional methods, broadening their potential applications.

## 1. Introduction

In the realm of additive manufacturing (AM), a technological evolution has broadened its application across diverse fields such as aerospace [1,2], automotive [3,4], military [5], and medicine [6–8]. Within this spectrum, Fused Filament Fabrication (FFF) has emerged as a notably versatile process. Its widespread adoption is attributed to factors like cost-efficiency, simplicity of the required equipment, and a safer printing process, as evidenced in its applications ranging from manufacturing parts [9–14] to biomedical models [15–17]. However, FFF's predominant layer-by-layer printing approach, involving molten filament extrusion, introduces significant challenges. This method results in limited bonding between adjacent layers, leading to reduced structural strength and diminished shear resistance in the build direction of the parts. These limitations present critical barriers to the advancement and broader application of FFF technology, signaling a need for innovation in layer bonding techniques to enhance the structural integrity of FFF-produced components.

Enhancing FFF technology to improve the mechanical properties of printed parts, particularly in terms of build direction strength and interlayer shear resistance, is a critical area of development. The strength of these interlayer bonds is largely determined by the degree of material diffusion at the cross-sectional interface, as explored by relevant researchers [18–20]. To this end, some studies have explored actively heating the print layer during deposition, using techniques like heated airflow [21] or thermal radiation [22,23]. In parallel, other research efforts have focused on post-processing techniques to strengthen interlayer bonds [24,25]. However, thermal operation approaches risk altering the part's original geometry. While post-processing strategies have been effective in enhancing mechanical properties at the interlayers, they entail additional material requirements. This ongoing exploration into both during- and post-printing techniques underscores the multifaceted approach needed to address the intrinsic limitations of FFF technology, aiming to expand its application potential by improving part strength and durability.

Only a few studies have considered utilizing the anti-deformation properties of interlayer structures to enhance the interlayer mechanical properties of 3D-printed parts. One particular study introduced a printing method that deposits "pins" on multiple layers throughout the interior of the part to enhance the interlayer mechanical properties [26]. Their experiments demonstrated the success of this method

---

## Nature-inspired interlaced printing strategies
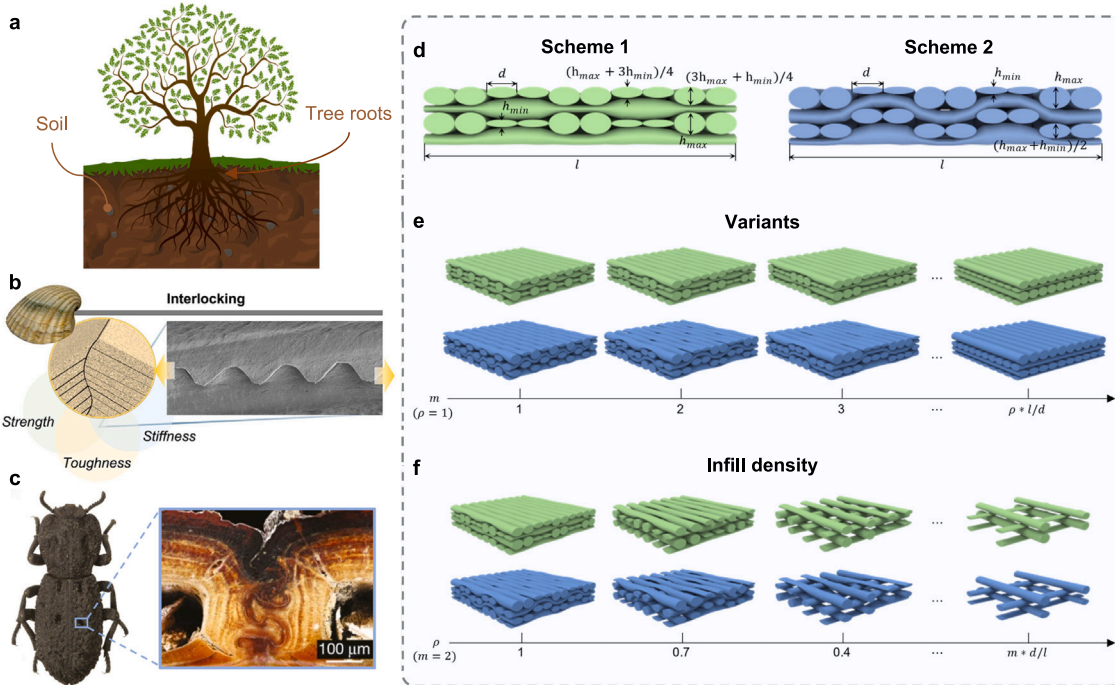


**Fig. 1.** **Schematics of the two different toolpath schemes.** **a** The roots of trees are deeply rooted in the ground to resist wind blowing. **b** Shells have excellent strength, stiffness and toughness [39]. **c** Beetles have tough joints and interfaces [40]. **d** is two schematic models of the two toolpath schemes. The green schematic model is Scheme 1 and the blue schematic model is Scheme 2. **e** is a schematic model of the toolpath for different parameters $m$ at 100% infill density. **f** is a schematic model of the toolpath for different infill densities with the parameter $m = 2$.

in some cases, although in others, samples without this treatment performed better. For non-planar toolpath methods, since each layer has a certain curvature, the mechanical properties between layers can theoretically be improved. Especially in multi-axis printers [27], due to the higher degree of freedom of the deposition heads of this type of printer, it is possible to print steeper toolpaths, which can effectively improve the mechanical properties between layers. At the same time, using the high flexibility of this printer, slicing can be performed based on the stress field to optimize the overall mechanical properties of the model [28]. However, considering the higher cost and not yet fully matured characteristics of multi-axis printers, the 3-axis printers have a lower cost and broader applications in terms of manufacturing compared to them. However, most of the current research for 3-axis printers with non-planar toolpath methods and curved layer slicing [29–31] has focused on relieving the case effect between layers [32–35] and support-free printing [36] to enhance the surface accuracy of the part and reduce material costs. Only very few studies have focused on enhancing the interlayer mechanical properties of the model such as 3D woven deposition toolpath [37] and ZigzagZ [38]. These methods are very effective in optimizing interlayer mechanical properties of printed parts on non-planar paths of 3-axis printers. However, the variety of this non-planar geometry is relatively simple, and more research may be needed to further enrich and optimize the methods in this field.

Bionic design, which seeks to enhance man-made structures by emulating biological ones found in nature, is an increasingly promising approach in structural engineering and materials science [41,42]. Nature offers a plethora of examples where mechanical interlocking structures bolster mechanical properties. For example, the roots of trees are deeply rooted in the ground to resist wind blowing (see Fig. 1a); the mineral platelets in natural perlite have a wavy cross-section, which leads to transverse interlocking between neighboring platelets, thus increasing the resistance to deformation of the composite material

against localized strains [43,44]; the individual lamellae of seashells exhibit a herringbone cross-interlocking structure between 30° and 40°, which renders them ultra-high strength and toughness [39] (see Fig. 1b); and the beetle's exoskeleton utilizes interlocking structures to have tough joints and interfaces [40,45] (see Fig. 1c); the mineralized microridges in the exoskeleton of sea urchins [46,47], and the toothed interlocking mineral shells of diatoms [48], to name a few. These similar structures play an important role in nature by helping organisms and objects to remain stable and robust in unstable environments, and occur frequently in nature to adapt to different environments and survival needs.

Here, we have drawn inspiration from nature to propose two nature-inspired interlaced printing toolpath planning schemes (see Fig. 1d). These schemes allow the deposition head to perform not only linear motion in the XY plane but also periodic intermittent motion in the Z-axis direction during the deposition process. Each period can be considered as a basic unit, and these units can be repeated while printing the model, regardless of the overall shape or size of the model. With fixed extrusion head apertures, we set the maximum printable layer thickness as $h_{max}$, the minimum printable layer thickness is defined as $h_{min}$, and the toolpath width is $d$.

In the toolpath of Scheme 1 (the green schematic model in Fig. 1d), the filament deposition rate of each layer is shown to vary. The maximum layer thickness for the first and last layers is set to $(3h_{max} + h_{min})/4$, while the minimum layer thickness is $(h_{max} + 3h_{min})/4$. The goal of this design idea is to fully utilize the range of middle layer thicknesses to accommodate variations in printable layer thicknesses (i.e., the maximum layer thickness for the middle layers is $h_{max}$ and the minimum layer thickness is $h_{min}$). In the toolpath of Scheme 2 (the blue schematic model in Fig. 1d), only the filament deposition rate of the first and last layers are shown to vary. The maximum layer thickness for the first and last layers is set to $h_{max}$, while the minimum layer
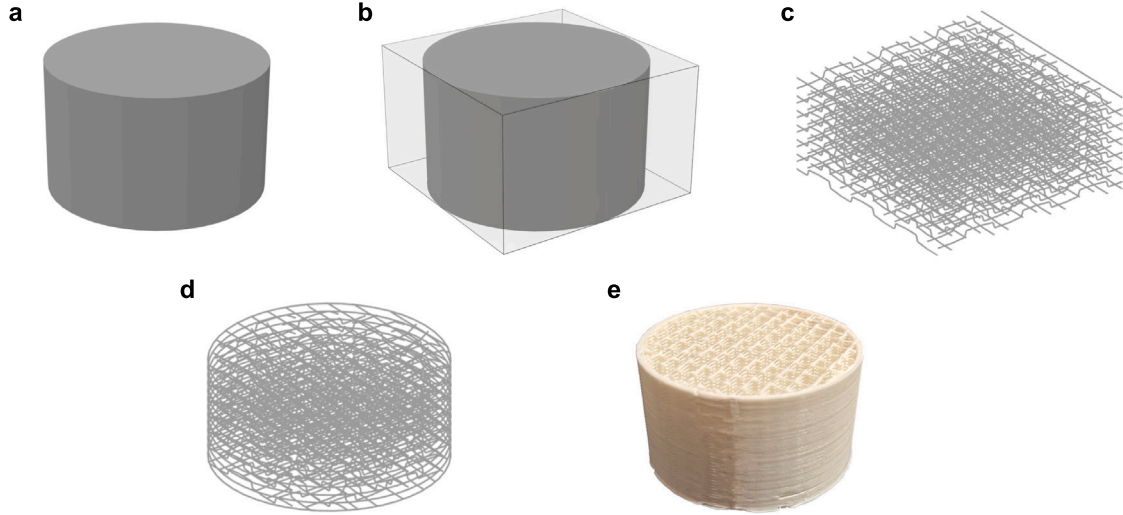
**Fig. 2. The pipeline of interlaced printing algorithm in this paper. a** is input model. **b** is the bounding box of the model. **c** is to generate the toolpaths with the same size as the bounding box. **d** is the infill pattern of the model. **e** shows the printed object filled with our schemes.

thickness is $h_{min}$. The layer thickness of the middle layer is constant as $(h_{max} + h_{min})/2$.

In addition, the variant of the proposed method was developed to analyze its effect (discussed in the following sections). The variant is controlled by the integer parameter $m$. As can be seen in Fig. 1e, at the same infill density $\rho$, the number of deposition head lifts in the $Z$-axis direction decreases as $m$ increases. If $m = \rho * l/d$, the infill toolpath will change to a planar toolpath. Therefore, the effective range of the parameter $m$ is $[1, \rho * l/d]$. Additionally, the proposed method can select the appropriate infill density for different models, which makes the printing process spend less time with less material consumption while obtaining enough mechanical strength. The effective range of the infill density $\rho$ is $(m * d/l, 1]$, as shown in Fig. 1f. A movie demonstrating the deposition sequence of the two schemes are provided as supplementary data (supplementary Movie S1).

## 2. Experiments and methods

### 2.1. Methods pipeline

In Fig. 2, we show the pipeline of interlaced printing algorithm in this paper. For a given 3D model (see Fig. 2a), we first generate the axis-aligned bounding box of this model (see Fig. 2b). Then, the model and the bounding box are sliced and a suitable scheme is selected to generate the toolpath (see Fig. 2c). Further on, a cropping algorithm is used to obtain the toolpaths inside the model contour (see Fig. 2d). Finally, the model was fabricated using a 3D printer (see Fig. 2e).

### 2.2. Interlaced toolpath generation

The two proposed schemes are mainly based on the improvement of traditional toolpaths. Take the interlaced one (see the upper part of Fig. 3) as an example. First, a Zigzag-filled toolpath with a certain infill density $\rho$ and layer thickness $(h_{max} + h_{min})/2$ is generated in the axis-aligned bounding box of the model, as shown in Fig. 3a. Then the points $P = \{p_{i,j,k} | 1 \leq i \leq X_{count}, 1 \leq j \leq Y_{count}, 1 \leq k \leq Z_{count}\}$ on the motion trajectory of the deposition head are extracted according to the infill density $\rho$ and toolpath width $d$ (see the red points in Fig. 3), where $Z_{count}$ is the number of layers, $X_{count}$ and $Y_{count}$ are the number of toolpath in $X$-axis and $Y$-axis directions. It is worth noting that the interval between the trajectory points increases with toolpath width $d$ and decreases with infill density $\rho$. Ensure that the X–Y coordinates of all trajectory point $P$ remain unchanged, and reset the $Z$-axis

coordinates $z(p_{i,j,k})$ according to the numbering to create a periodic interlaced toolpath. The specific realization details are as follows:

The trajectory points are divided into three parts by the slicing layer: the first layer trajectory points, the middle layer trajectory points, and the last layer trajectory points. For Scheme 1, the reset $Z$-axis coordinates of the first layer trajectory points $z(p_{i,j,1})$ are:

$$z(p_{i,j,1}) = \begin{cases} (h_{max} + 3h_{min})/4, & \text{if } (\lfloor (i-1)/m \rfloor + \lfloor (j-1)/m \rfloor + 1)\%2 \neq 0 \\ (3h_{max} + h_{min})/4, & \text{otherwise,} \end{cases}$$

(1)

where the number of reset trajectory points in each group can be controlled by adjusting the parameter $m$. The reset $Z$-axis coordinates of the middle layer trajectory points $z(p_{i,j,k})$ are:

$$z(p_{i,j,k}) = \begin{cases} z(p_{i,j,k-1}) + h_{min}, & \text{if } (\lfloor (i-1)/m \rfloor + \lfloor (j-1)/m \rfloor + k)\%2 \neq 0 \\ z(p_{i,j,k-1}) + h_{max}, & \text{otherwise.} \end{cases}$$

(2)

The reset $Z$-axis coordinates of the last layer trajectory points $z(p_{i,j,k})$ are:

$$z(p_{i,j,k}) = \begin{cases} z(p_{i,j,k-1}) + (h_{max} + 3h_{min})/4, & \text{if } (\lfloor (i-1)/m \rfloor \\ \qquad\qquad + \lfloor (j-1)/m \rfloor + k)\%2 \neq 0 \\ z(p_{i,j,k-1}) + (3h_{max} + h_{min})/4, & \text{otherwise.} \end{cases}$$

(3)

For Scheme 2, the reset $Z$-axis coordinates of the first layer trajectory points $z(p_{i,j,1})$ are:

$$z(p_{i,j,1}) = \begin{cases} h_{min}, & \text{if } (\lfloor (i-1)/m \rfloor + \lfloor (j-1)/m \rfloor + 1)\%2 \neq 0 \\ h_{max}, & \text{otherwise.} \end{cases}$$

(4)

Different from Scheme 1, the thickness of the middle layer for Scheme 2 is constant, so the reset $Z$-axis coordinates of the middle layer trajectory point $z(p_{i,j,k})$ are:

$$z(p_{i,j,k}) = z(p_{i,j,k-1}) + (h_{max} + h_{min})/2.$$

(5)

At the same time, when the trajectory points have the same $i - j$ numbering, the $Z$-axis increment for the last layer of trajectory points is opposite to that of the first layer. Therefore, the reset $Z$-axis coordinates of the last layer trajectory points $z(p_{i,j,k})$ are:
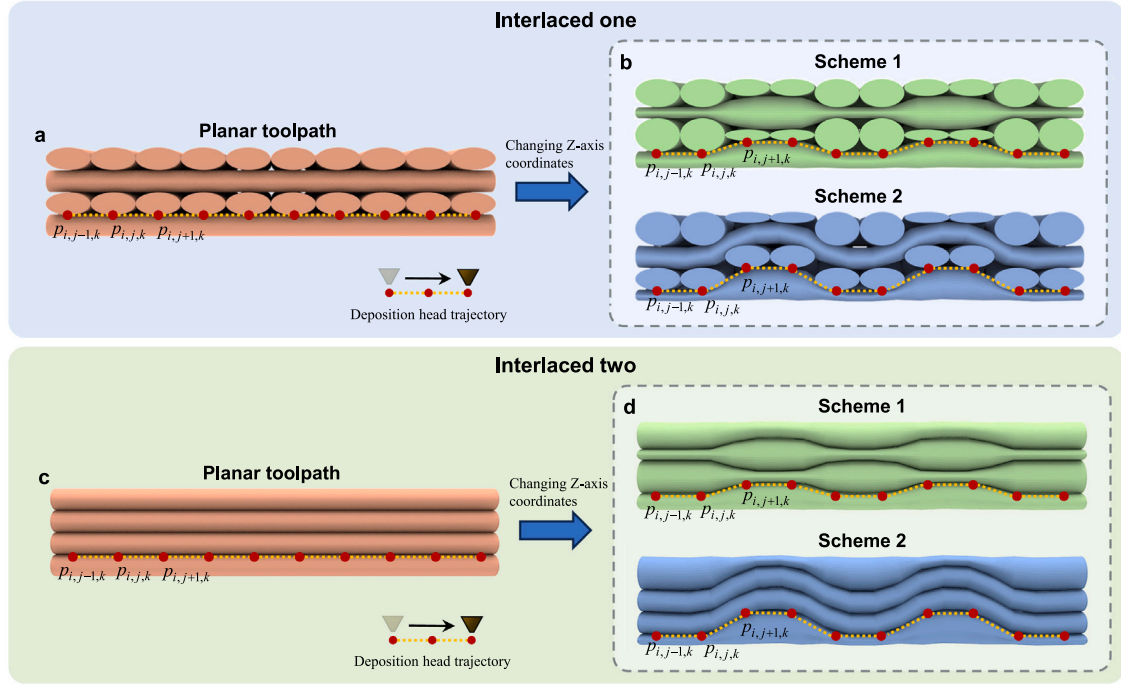
**Fig. 3. The schematic of the two schemes generated.** The upper half presents Interlaced one, where the toolpath direction alternates by 90° layer by layer. The lower half presents Interlaced two, where the toolpath direction remains consistent without alternating layer by layer. **a** and **c** are traditional planar toolpath. **b** and **d** are the two schemes generated after resetting the $Z$-axis coordinates of the trajectory points.
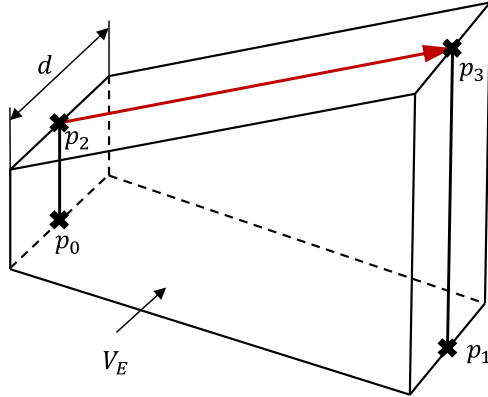


**Fig. 4. The schematic of the extrusion parameters.** The red arrow indicates the movement of the deposition head. (For interpretation of the references to color in this figure legend, the reader is referred to the web version of this article.)

$$z(p_{i,j,k}) = \begin{cases} z(p_{i,j,k-1}) + h_{max}, & \text{if } (\lfloor (i-1)/m \rfloor + \lfloor (j-1)/m \rfloor + 1)\%2 \neq 0 \\ z(p_{i,j,k-1}) + h_{min}, & \text{otherwise.} \end{cases}$$

$$(6)$$

Interlaced two (see the lower part of Fig. 3) is a printing pattern where the toolpath direction does not alternate layer by layer. It is generated in a similar way to Interlaced one.

### 2.3. Calculating the extrusion value

After obtaining the interlaced toolpath, the corresponding material extrusion $E$ should also be updated. This can be controlled by the extrusion rate [49,50]. For the calculation of the extrusion rate, we refer to the work of Pelzer et al. [34]. Fig. 4 shows one of the volumetric elements in the middle layer of Scheme 1 when the deposition head

rises for printing, and the volume equation is shown below:

$$V_E = \frac{1}{2} \cdot d_{sp} \cdot d \cdot \left( -z\left(p_0\right) - z\left(p_1\right) + z\left(p_2\right) + z\left(p_3\right) \right), \qquad (7)$$

where, $V_E$ is volume of volumetric element, $d_{sp}$ is euclidian distance in the XY-plane between support points $p_2$ and $p_3$, $d$ is the width of the extruded toolpath, $z(p_{0\sim3})$ is Z-coordinates of points $p_0$ to $p_3$. The volume of material entering the printer can be calculated based on the cylindrical formula:

$$V_F = \pi \cdot \frac{D_F^2}{4} \cdot E, \qquad (8)$$

where, $V_F$ is the volume of material consumed, $D_F$ is diameter of material filament, $E$ is squeeze-in length of material. Since the volume of material consumed $V_F$ by the printer is equal to the volume extruded $V_E$, the extruded length of material $E$ in the process of deposition head from $p_2$ to $p_3$ can be found according to the Eq. (9).

$$E = \frac{2 \cdot d_{sp} \cdot d}{\pi \cdot D_F^2} \cdot \left( -z\left(p_0\right) - z\left(p_1\right) + z\left(p_2\right) + z\left(p_3\right) \right). \qquad (9)$$

It is worth noting that these calculations also apply to other scenarios, such as planar printing (i.e., $z(p3) - z(p1) = z(p2) - z(p0)$), and these computations were conducted in discrete steps. We further subdivided the trajectory points with an interval of $d/8$ when raising and lowering the deposition head during printing. This is done to ensure that the correct amount of material is extruded for each calculated section. At the same time, approximating the toolpath cross-section as a rectangle can be a good way to bond neighboring toolpaths together.

### 2.4. Constraint on the slope angle

The collisions that can occur when the deposition head up and down to print are different [51] (see Fig. 5). We simplify the deposition head as a truncated cone (depicted in brown) to calculate the angle. As the deposition head is up to print (left), it may collide with the printed part. Assuming that the reference layer thickness $h$ and deposition
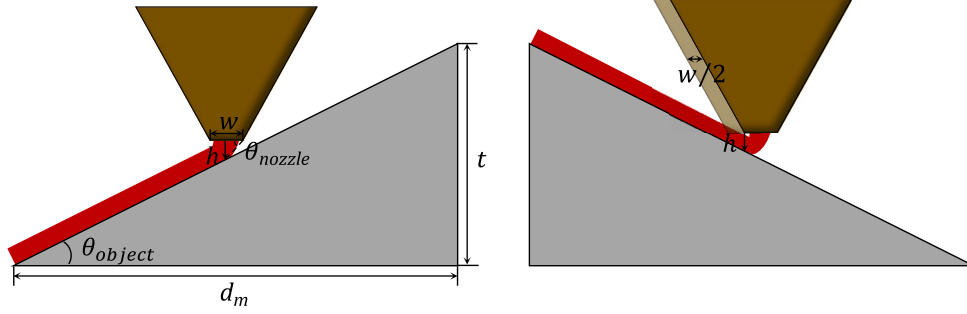
**Fig. 5.** Constraint on the slope angle of the interlaced printing toolpath.

head aperture $w$ are constant, the height $t$ and length $d_m$ of the up should be controlled to avoid collisions, i.e., $\theta_{object} < \theta_{nozzle}$, where $\theta_{object} = \tan^{-1} \frac{t}{d_m}$, $\theta_{nozzle} = \tan^{-1} \frac{2h}{w}$. As the deposition head down to print (right), it collides with the current layer, creating a "plow" effect. This phenomenon causes the thickness of the toolpath layer to be less than the predefined thickness. To address this issue, it is necessary to offset the deposition head by a distance of $w/2$. Note that the "plow" effect does not disappear for non-planar printing on the 3-axis printer, but is mitigated as the slope decreases until it disappears for planar printing.

### 2.5. Implementation details

These test specimens in this paper included toolpath geometry using a four-sided hollow box consisting of stacked monolayers. Bridge model was used for the traditional compression test. Dogbone model was used for the traditional tensile test. Our specially designed model was used for shear tests, and a rectangular model was used for bonding tests. To ensure the fairness of the tests, none of these models were generated with the shell contour, the dimensions of which are shown in Fig. 6.

The proposed algorithm was implemented with C++. All experiments were carried out on a laptop, which adopts AMD Ryzen 7 4800H with Radeon Graphics @ 2.90 GHz + 16 GB RAM. The shell contour toolpath is generated by the graphic processing library ClipperLib [52]. For the changing extrusion rate in non-planar layers, we refer to the work of Pelzer et al. [34] (see Section 2.3). We designed the program to be very simple to operate. Just import an STL or OBJ file into the program and set a series of parameters. These parameters include the parameter $m$, the filling density $\rho$, whether or not the outer contour and support are needed, and so on. After clicking Run, the program automatically slices and generates a G-Code file that the printer can recognize.

### 2.6. Fabrication and measurement

All objects were fabricated using the CR-10S 3D printer, as shown in Fig. 7c. Its working space is 300 mm × 300 mm × 400 mm, the printing material was Polylactic Acid (PLA) (Creality 3D branded). For the selection of deposition heads, it is obvious that different diameter deposition heads can generate toolpaths with different layer thickness intervals. A general rule of thumb is that the maximum layer thickness should stay within $[0.1w, 0.75w]$ where $w$ is the deposition head diameter. This gives from 0.04 mm to 0.3 mm for a typical 0.4 mm deposition head [29]. In this paper, there are no restrictions on the size of the deposition head used. However, to make the interlayer pattern more significant, we use a 0.8 mm diameter of the deposition head and allow layer thicknesses from 0.6 mm down to 0.2 mm (i.e., $h_{max} = 0.6$ mm and $h_{min} = 0.2$ mm). The deposition head temperature was set to $210°C$ and the print bed temperature was set to $50°C$. To ensure the stability of the printer during operation, the acceleration of the XYZ-axes was 500 mm/s², 500 mm/s², and 100 mm/s², respectively, and the

maximal speed was 500 mm/s, 500 mm/s, and 10 mm/s, respectively. We determined the dimensions of the tensile specimens (Dogbone) according to the standards ISO 527-1:2019 and ISO 527-2:2012.

For shear and bonding tests, an electronic universal testing machine from Changchun New Testing Machine Co., Ltd. was used, with an extension speed of 1 mm/min. For conventional tensile and compression tests, a Handpi HSV universal electric testing machine was used, with an extension speed of 60 mm/min. To observe the geometry features of the toolpath and the fracture of the damaged specimens, we chose a 3D video microscope (Leica DVM6).

## 3. Results and discussion

### 3.1. Geometric features

The toolpaths performed by the two schemes were microanalyzed to determine the effect of the proposed method on the toolpath geometry. The test objects are two schemes with different parameters $m$ and rated speeds $v$, the toolpath width is set to 0.8 mm and the average layer thickness is 0.4 mm. As shown in Fig. 7a, from left to right in each sub-figure are the rising print stage, the planar print stage, and the falling print stage, respectively. As a whole, the filament deposition process of these two schemes resulted in a special structure with toolpaths similar to the geometry of a "dumbbell". Through experiments, we observe that the deposition head moves slower in the $Z$-axis direction than in the plane direction due to the printer being driven by a screw mechanism in the $Z$-axis direction, as shown in Fig. 7c. It may be the main reason for the "dumbbell" shape. At the same time, it can be seen that the toolpath printed when the deposition head is falling is wider than when it is rising. This is because the outer wall of the deposition head collides with the toolpath when it is descending, thus creating a "plow" effect on the toolpath, as can be seen in Fig. 7b. It is worth noting that in Section 2.4 we only ensure that the layer thickness is consistent with the preset thickness when printing downwards, but the "plow" phenomenon cannot be avoided for non-planar printing on the 3-axis printer. However, it can be mitigated by reducing the infill density $\rho$ of the print to slow down the slope of the deposition head as it rises and falls, thus reducing the extent of collision between the deposition head and the toolpath.

To further investigate the specific reasons for the "dumbbell" geometry, the speed curves were statistically plotted, as shown in Fig. 7d. It can be seen that when $m = 2$, the deposition head accelerates before reaching the rated speed $v$ to decelerate because the distance is too short. Therefore, the speed curve is the same at two different rated speeds, and the toolpath geometry in Fig. 7a does not change. And when $m = 4$ and 6, the maximum moving speed is affected by the rated speed $v$ and goes through the process of acceleration, uniform speed, deceleration, and stopping. It can be clearly seen from the toolpath geometry and width range (PWR) that the formation of the "dumbbell" shape can be relieved by controlling the maximum moving speed.

In addition, during the filament deposition process, there is a delay between the material extruded by the extrusion wheel and the extrusion
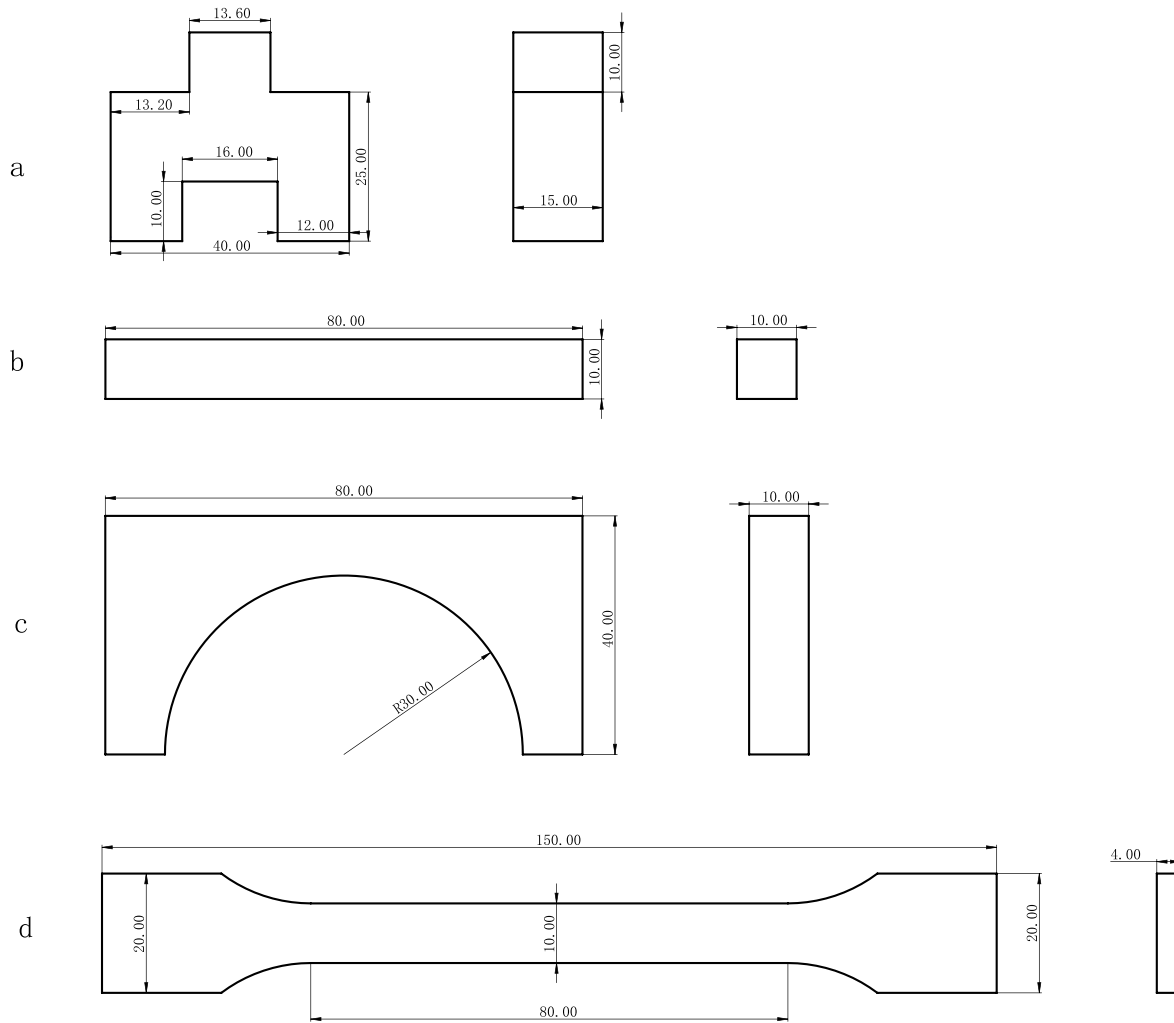
**Fig. 6. Specimens for mechanical property testing (unit: mm). a** Specimens we designed for shear testing. **b** Specimens for interlayer bonding tests. **c** Specimens for conventional compression testing. **d** Specimens for conventional tensile testing.

head, which also has an effect on the toolpath geometry [53]. From the perspective of the toolpath geometries of the two schemes (see Fig. 7a), the "dumbbell" shape in the toolpath geometry of Scheme 1 is more significant compared to Scheme 2 because the extrusion rate of Scheme 1 in the middle layer is constantly changing (the interlayer gap is also affected in the same way, as shown in Fig. 8). It is also for this reason that it is difficult to relieve the "dumbbell" shape by dynamically adjusting the extrusion rate. While this particular structure will have some impact on fabrication time and model accuracy, it may provide some mechanical property benefits to the interlayer region. This feature helps to increase the cross-sectional area, thus improving the bonding between layers.

### 3.2. Enhancement of shear properties

In this section, we performed a comparison of the mechanical properties of the two schemes and the conventional planar toolpath. In this comparison, we set all configurations to 100% infill density, the average layer thickness is 0.4 mm, and the toolpath width is 0.8 mm, the rated print speed is kept at 40 mm/s.

A specimen was designed with the building orientation shown in Fig. 9a. This specimen can simulate a shear test by simply fixing the bottom and sides and pressurizing the top. This design allows us to perform the shear performance test on a conventional pressure tester. Meanwhile, to deeply analyze the performance of the proposed

method under different parameters $m$, we designed three groups of 11 specimens each, covering the toolpaths of $m = 2$, $m = 4$, $m = 6$, $m = 8$, $m = 10$ under the two schemes, and the conventional planar toolpath. The printed specimens of the two proposed schemes under different parameters $m$ are shown in Fig. 9b.

The force–strain curves of the printed specimen are shown in Fig. 9c, which is divided into three stages. In the first stage, the deformation of the specimen is proportional to the force when the force is less than the material's elastic limit. The specimen exhibits elastic deformation in this stage, i.e., it can be restored to its original state after the force is removed. In the second stage, the strain increases significantly, breaking the original linear relationship between the force and strain, which is mainly affected by the bonding force between layers. When a certain force value is reached, the bond fails and the specimen printed by the planar toolpath method reaches the maximum load-bearing capacity before failure. However, the proposed method introduces a third stage, as clearly demonstrated in the force–strain curve, where the specimen's performance is significantly enhanced. In contrast, the planar toolpath algorithm does not exhibit such a phase change.

The reason for this phenomenon is that when a force is applied to the specimen printed by the proposed method, the strain resistance of the structure comes into play, in addition to the effect of the bonding forces between the layers. This can be likened to the "protrusions" between the layers, which share the forces to a certain extent. At the same time, as $m$ decreases, the number of "protrusions" increases, and
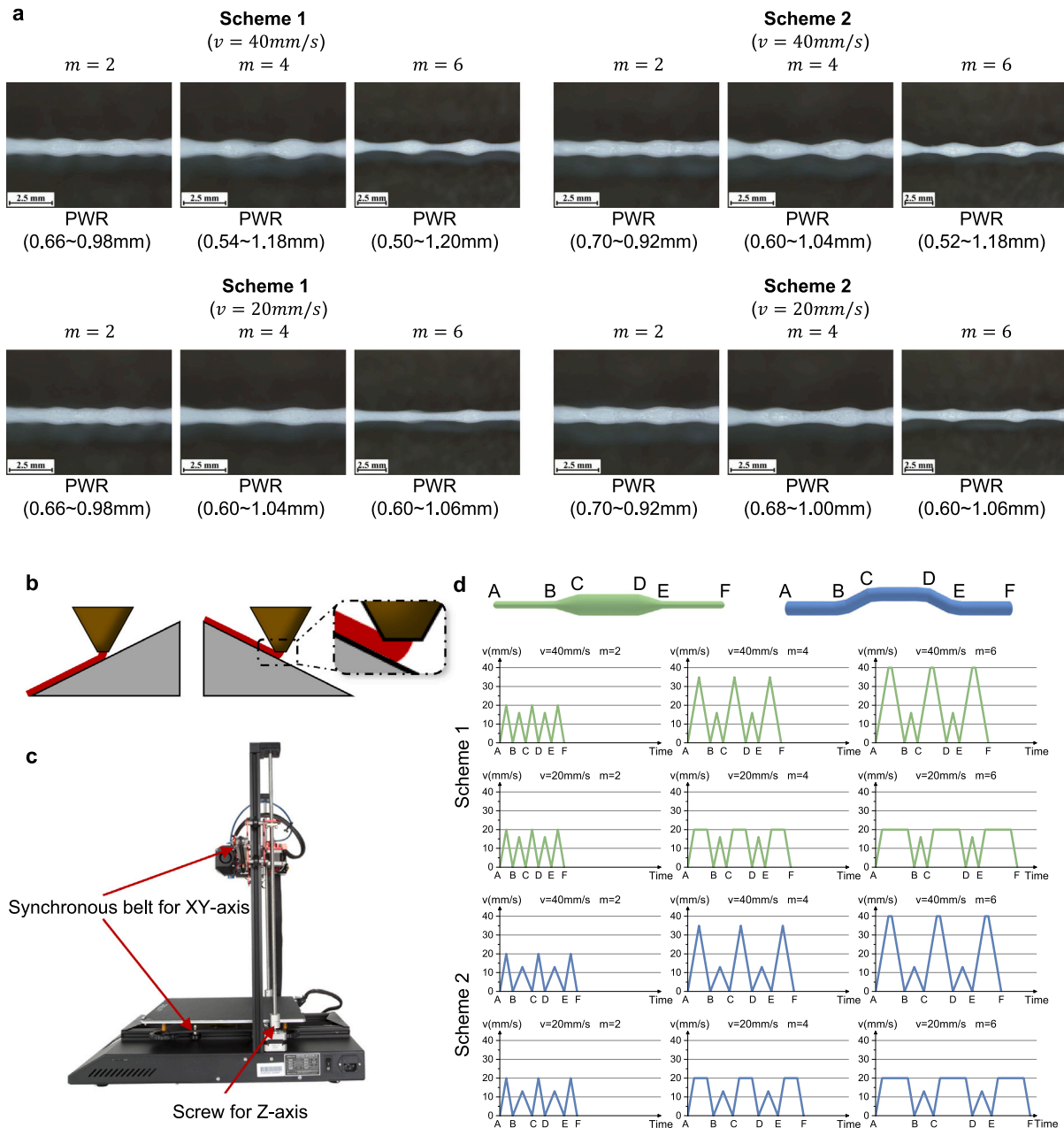
**Fig. 7. Effect of the proposed method on resulting specimen geometry. a** is the toolpath geometry of the two schemes, from left to right in each subfigure are the rising print stage, the planar print stage, and the falling print stage, respectively. Also, the path width range (PWR) is given below each subfigure. **b** Comparison of rising print (left) and falling print (right) of the deposition head during deposition. **c** is a common FFF 3D printer. The transmission device of the $Z$-axis is usually a screw, while that of the XY-axis is usually a synchronous belt. **d** is the print speed curves of the deposition head running at different schemes and rated speed $v$.

thus the share of force increases. As shown in the third stage of the force–strain curve, the specimen's stiffness and maximum load-bearing capacity gradually increase as $m$ decreases.

The histograms of each property are shown in Fig. 9d. It can be seen that the two proposed schemes have higher mechanical properties than the planar toolpath method. Among them, the strength (breaking force) and fabrication time decrease with increasing $m$, which may be related to the number of "protrusions". Ductility (fracture strain) and toughness exhibit a normal distribution. These performance metrics peak when $m = 6$. In addition, Scheme 1 is lower than Scheme 2 in all properties, which may have much to do with the printer delay, as described in Section 3.1.

In summary, although the two proposed schemes have longer fabrication times than conventional planar toolpaths in shear tests, they

significantly improve several performance metrics, such as the specimens' strength, toughness, and ductility. Among them, Scheme 2 demonstrates significant improvements, with strength, toughness, and ductility increasing by 67.5%, 92.2%, and 47.1%, respectively. In contrast, Scheme 1 exhibits corresponding improvements of 31.9%, 89.9%, and 47.5%.

### 3.3. Mechanical analysis of interlayer bonding

The proposed method produces a special "dumbbell" geometry which may increase the interlayer bonding. To verify this conjecture, a rectangular specimen with a length and width of 10 mm and a height of 80 mm will be used in this section (see Figs. 10a and 6b). Due to the small diameter of the specimen, each test is divided into three groups,
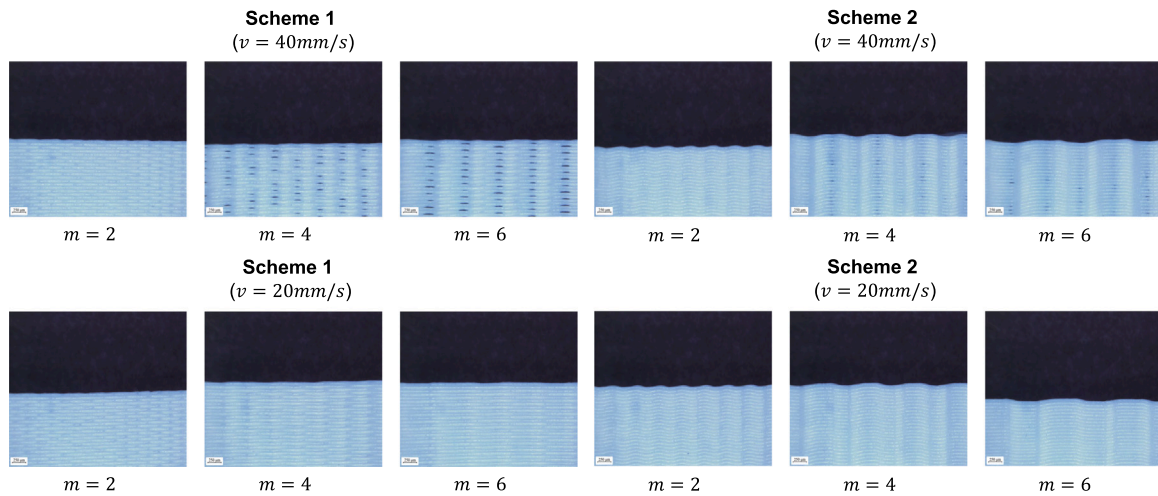
**Fig. 8.** The toolpath thickness geometries of the two schemes with different parameters.
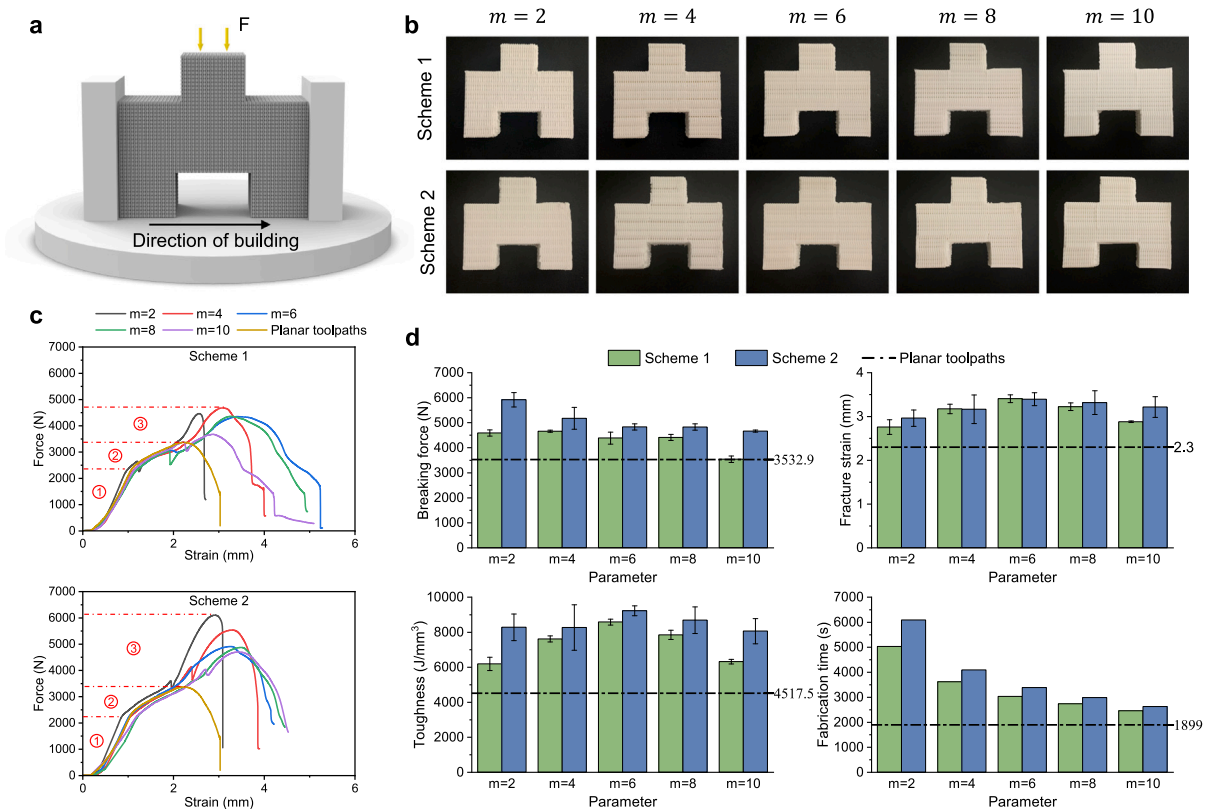


**Fig. 9. The shear properties of the specimen printed by the proposed method. a** We have designed a specimen that can be tested for shear performance on a normal pressure tester by simply fixing the sides. **b** Some of the specimens printed by the proposed method. **c** The shear force–strain curves of printed specimens. **d** Histogram of the different properties of printed specimens.

and each group consists of the toolpath of $m = 2$, $m = 4$, $m = 6$ under the two schemes, and the planar toolpath. Fig. 10b illustrates the histogram of the test data. It can be seen that the strength of both specimens is higher than that of the conventional planar toolpath and shows a normal distribution with different $m$. However, the ductility and toughness performance of Scheme 2 is significantly weaker. This may be due to the deposition head's downward movement during the printing of each layer's toolpath, resulting in a compression effect of the current layer's toolpath on the previous layer's toolpath, which

enhances the interlayer bonding but also reduces the toughness and ductility of the specimen. This phenomenon is confirmed by the trend of increasing toughness and ductility with increasing $m$. Furthermore, Scheme 1 has a gap between layers due to the changing extrusion rate. Thus, the performance improvement is not significant.

In summary, in the interlayer bonding test, the proposed method has a stronger bonding than the planar toolpath, which can enhance the strength and stiffness of the specimen. However, the corresponding ductility and toughness are reduced.
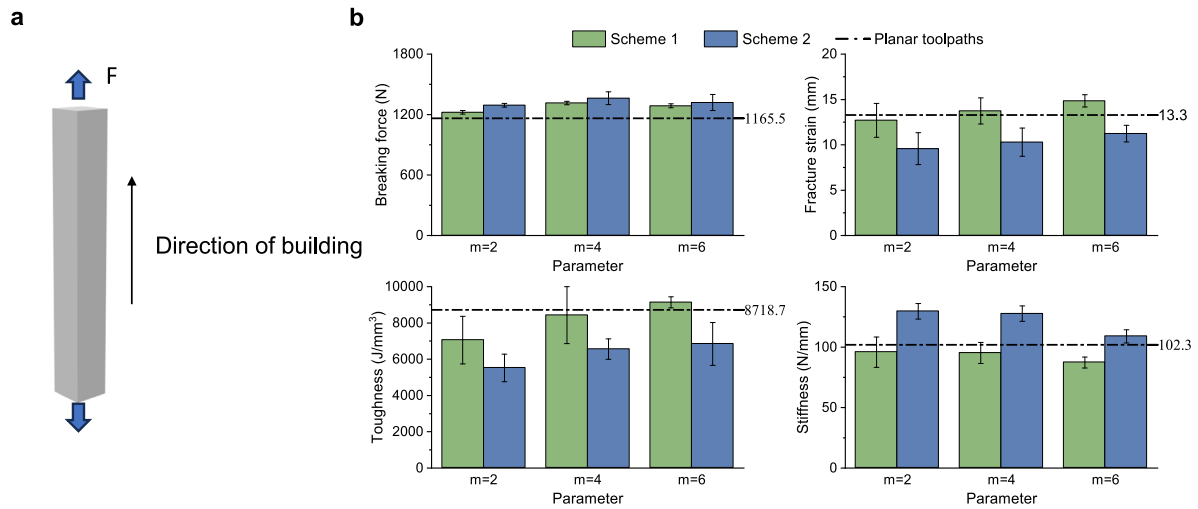
**Fig. 10. The interlayer bonding properties of the specimen printed by the proposed method. a** Interlayer bonding test specimen. **b** Histogram of the different properties of printed specimens.
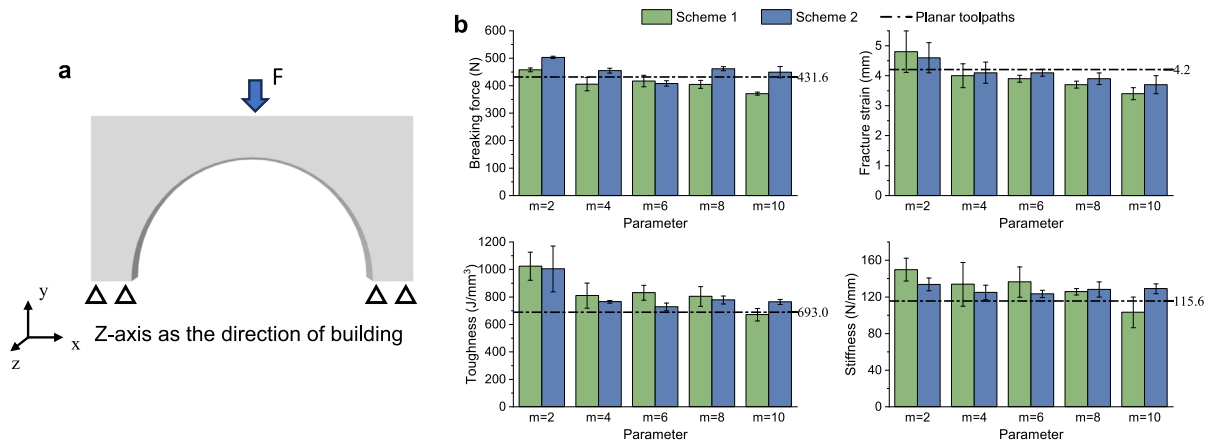


**Fig. 11. The compression properties of the specimens printed by the proposed method. a** The bridge model for compression testing, and the direction of building is *Z*-axis. **b** Histogram of the different properties of printed specimens.

### 3.4. Mechanical analysis of planar compression and tension

To evaluate whether the toolpaths generated by the proposed method have an impact on conventional compression and tensile performance. We used the Bridge model and the Dogbone model (see Fig. 11a and Fig. 12a) for the compression and tensile experiments, respectively (the building direction along the *Z*-axis for both models). The toolpath is planned using an alternating Zigzag 0° and Zigzag 90° pattern, the infill density of all samples is 100%, the toolpath width is 0.8 mm, the average layer thickness is 0.4 mm, and the rated travel speed of the deposition head is 40 mm/s.

The average effective strength, fracture strain, stiffness, and toughness of all specimens are shown in Figs. 11b and Fig. 12b, and the corresponding statistics are listed in the Tables 1 and 2. Compared with the conventional planar toolpath specimens, the average maximum effective strength increased by 6.0% and 16.7%, the fracture strain increased by 17.1% and 12.5%, the stiffness increased by 29.6% and 15.7%, and the toughness increased by 47.7% and 44.9% for Scheme 1 and 2, respectively, under compression environment. In the tensile environment, the average maximum effective strength increased by 27.1% and 57.6%, fracture strain increased by 21.1% and 43.1%, stiffness increased by 22.7% and 35.4%, and toughness increased by 74.8% and 151% for Scheme 1 and 2, respectively.

As mentioned above, in both experimental environments, the mechanical properties of our two proposed schemes show significant improvement compared to the planar toolpath approach, especially in terms of toughness. This is due to the fact that the wave-like shaped toolpaths are able to uniformly disperse the stress and absorb the energy when subjected to a force, thus improving the toughness and fracture resistance of the model. In addition, this phenomenon is more significant in the tensile test because the direction of the load is aligned with the direction of the toolpath. Considering that the magnitude of the up and down of the toolpath is greater in Scheme 2 than in Scheme 1, and that Scheme 1 is affected by printing delays, Scheme 2 almost always outperforms Scheme 1 in terms of mechanical property enhancement. At the same time, since the deposition head moves slower in the Z-direction, this results in longer print times and possible extrusion of excess material, see Tables 1 and 2. As seen in the result, the fabrication time of Scheme 2 is longer than that of Scheme 1, while the fabrication time of both schemes tends to decrease with the increase of *m*. However, both longer the planar toolpath algorithm regarding fabrication time. The material consumption is similar.

In summary, these results show that our two proposed schemes perform more prominently in terms of mechanical properties compared to the conventional planar toolpath, but require more printing time and material.
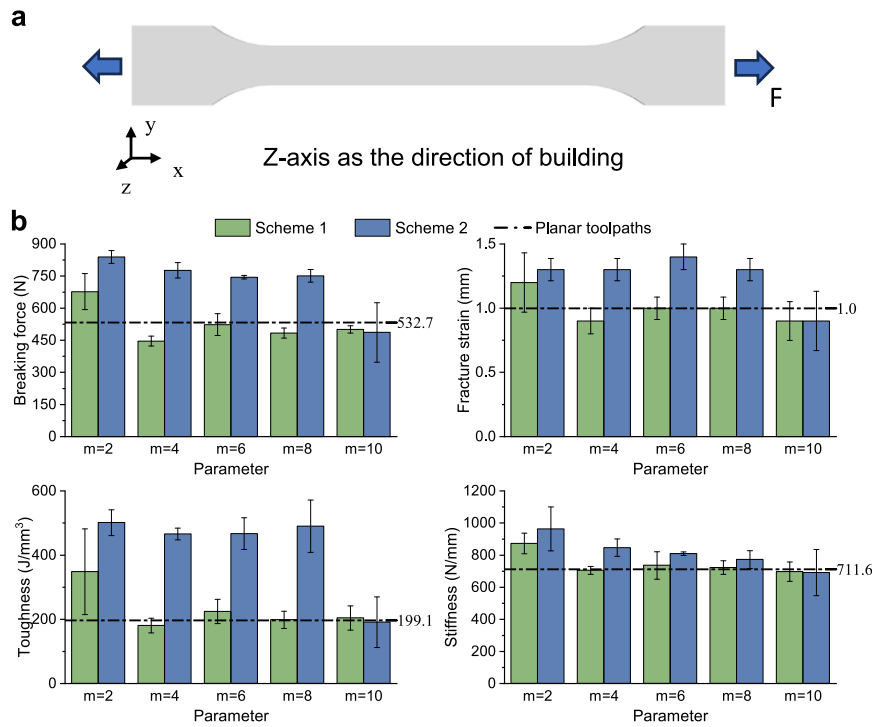
**Fig. 12. The tension properties of the specimens printed by the proposed method. a** The dogbone model for stretching testing, and the direction of building is *Z*-axis. **b** Histogram of the different properties of printed specimens.

**Table 1**
The statistics of all physical tests for Scheme 1 (averaged across three trials).

| Project | Infill pattern | Breaking force (N) | Fracture strain (mm) | Stiffness (N/mm) | Toughness (J/mm³) | Filament consumption (g) | Fabrication time (sec.) |
|---|---|---|---|---|---|---|---|
| Shear | m=2 | 4591.7 | 2.8 | – | 6191.8 | 16.8 | 5077 |
| | m=4 | 4660.9 | 3.2 | – | 7613.2 | 16.3 | 3660 |
| | m=6 | 4388.0 | 3.4 | – | 8577.2 | 16.4 | 3080 |
| | m=8 | 4414.8 | 3.2 | – | 7848.2 | 16.4 | 2791 |
| | m=10 | 3541.3 | 2.9 | – | 6316.2 | 16.2 | 2507 |
| | Planar toolpaths | 3532.9 | 2.3 | – | 4517.5 | 16.5 | 1956 |
| Bonding | m=2 | 1222.1 | 12.7 | 95.9 | 7056.5 | 7.9 | 2345 |
| | m=4 | 1314.8 | 13.7 | 95.1 | 8426.8 | 7.8 | 1607 |
| | m=6 | 1287.0 | 14.8 | 87.3 | 9132.7 | 7.7 | 1282 |
| | Planar toolpaths | 1165.5 | 13.3 | 102.3 | 8718.7 | 8.0 | 943 |
| Compression | m=2 | 457.7 | 4.8 | 149.8 | 1023.9 | 19.8 | 5456 |
| | m=4 | 405.7 | 4.0 | 133.8 | 809.2 | 19.8 | 3885 |
| | m=6 | 416.8 | 3.9 | 136.3 | 830.3 | 19.7 | 3219 |
| | m=8 | 404.7 | 3.7 | 125.7 | 803.5 | 19.5 | 2888 |
| | m=10 | 371.0 | 3.4 | 103.2 | 670.6 | 19.6 | 2529 |
| | Planar toolpaths | 431.6 | 4.1 | 115.6 | 693.0 | 19.8 | 1790 |
| Tensile | m=2 | 677.3 | 1.2 | 872.7 | 348.2 | 7.8 | 2294 |
| | m=4 | 466.3 | 0.9 | 704.9 | 180.7 | 7.6 | 1821 |
| | m=6 | 523.3 | 1.0 | 735.8 | 224.5 | 7.6 | 1661 |
| | m=8 | 484.0 | 1.0 | 722.6 | 198.6 | 7.6 | 1603 |
| | m=10 | 501.0 | 0.9 | 696.8 | 204.3 | 7.6 | 1525 |
| | Planar toolpaths | 532.7 | 1.0 | 711.6 | 199.1 | 8.3 | 1363 |

### 3.5. Fractographic analysis

The fracture surfaces of the specimens were observed using a 3D video microscope, as shown in Fig. 13. For the shear test (see Fig. 13a), the planar toolpaths of the fabricated samples showed flat fracture surfaces and tiny gaps between adjacent toolpaths could be observed. Only the edges of the cross-section show some fracture marks, which is due to the slowing down of the deposition head during the turn, resulting in the extrusion of excess material, and making the end portions of the neighboring toolpaths tighter. The two schemes we propose have an equal number of bulges for the same parameters *m*.

However, since the bulges are more prominent in Scheme 2, it has a stronger resistance to shear, which can be seen from the roughness of both sections. On the other hand, the destruction of the structure requires additional energy to be driven, which requires the application of higher loads compared to the planar toolpath approach that only destroys the interlayer bond. This is the reason why both of our schemes can provide stronger mechanical properties.

In the bonding test (see Fig. 13b), due to the principle of additive manufacturing layer-by-layer stacking, the mechanical properties are mainly affected by the interlayer bonding force. The magnitude of the interlayer bonding force is related to the tightness and contact area of

**Table 2**
The statistics of all physical tests for Scheme 2 (averaged across three trials).

| Project | Infill pattern | Breaking force (N) | Fracture strain (mm) | Stiffness (N/mm) | Toughness (J/mm³) | Filament consumption (g) | Fabrication time (sec.) |
|---|---|---|---|---|---|---|---|
| Shear | m=2 | 5917.0 | 3.0 | – | 8279.1 | 17.5 | 6136 |
| | m=4 | 5177.1 | 3.2 | – | 8265.6 | 17.0 | 4194 |
| | m=6 | 4832.4 | 3.4 | – | 9226.0 | 16.8 | 3434 |
| | m=8 | 4828.0 | 3.3 | – | 8683.2 | 16.6 | 3034 |
| | m=10 | 4666.9 | 3.2 | – | 8059.2 | 16.5 | 2677 |
| | Planar toolpaths | 3532.9 | 2.3 | – | 4517.5 | 16.5 | 1956 |
| Bonding | m=2 | 1292.1 | 9.6 | 129.6 | 5519.5 | 8.1 | 2831 |
| | m=4 | 1362.6 | 10.3 | 127.7 | 6557.5 | 8.0 | 1799 |
| | m=6 | 1319.3 | 11.2 | 108.9 | 6845.8 | 7.7 | 1375 |
| | Planar toolpaths | 1165.5 | 13.3 | 102.3 | 8718.7 | 8.0 | 943 |
| Compression | m=2 | 503.1 | 4.6 | 133.7 | 1004.2 | 21.5 | 6335 |
| | m=4 | 454.9 | 4.1 | 124.9 | 764.8 | 20.7 | 4433 |
| | m=6 | 408.1 | 4.1 | 123.3 | 727.6 | 20.5 | 3570 |
| | m=8 | 461.8 | 3.9 | 128.2 | 778.6 | 20.4 | 3134 |
| | m=10 | 449.1 | 3.7 | 129.0 | 764.0 | 20.0 | 2677 |
| | Planar toolpaths | 431.6 | 4.1 | 115.6 | 693.0 | 19.8 | 1790 |
| Tensile | m=2 | 839.3 | 1.3 | 963.2 | 501.0 | 9.2 | 2816 |
| | m=4 | 776.7 | 1.3 | 846.2 | 465.7 | 8.8 | 2086 |
| | m=6 | 744.7 | 1.4 | 809.4 | 466.8 | 8.6 | 1839 |
| | m=8 | 751.0 | 1.3 | 772.6 | 489.9 | 8.6 | 1749 |
| | m=10 | 486.7 | 0.9 | 690.9 | 191.0 | 8.6 | 1627 |
| | Planar toolpaths | 532.7 | 1.0 | 711.6 | 199.1 | 8.3 | 1363 |
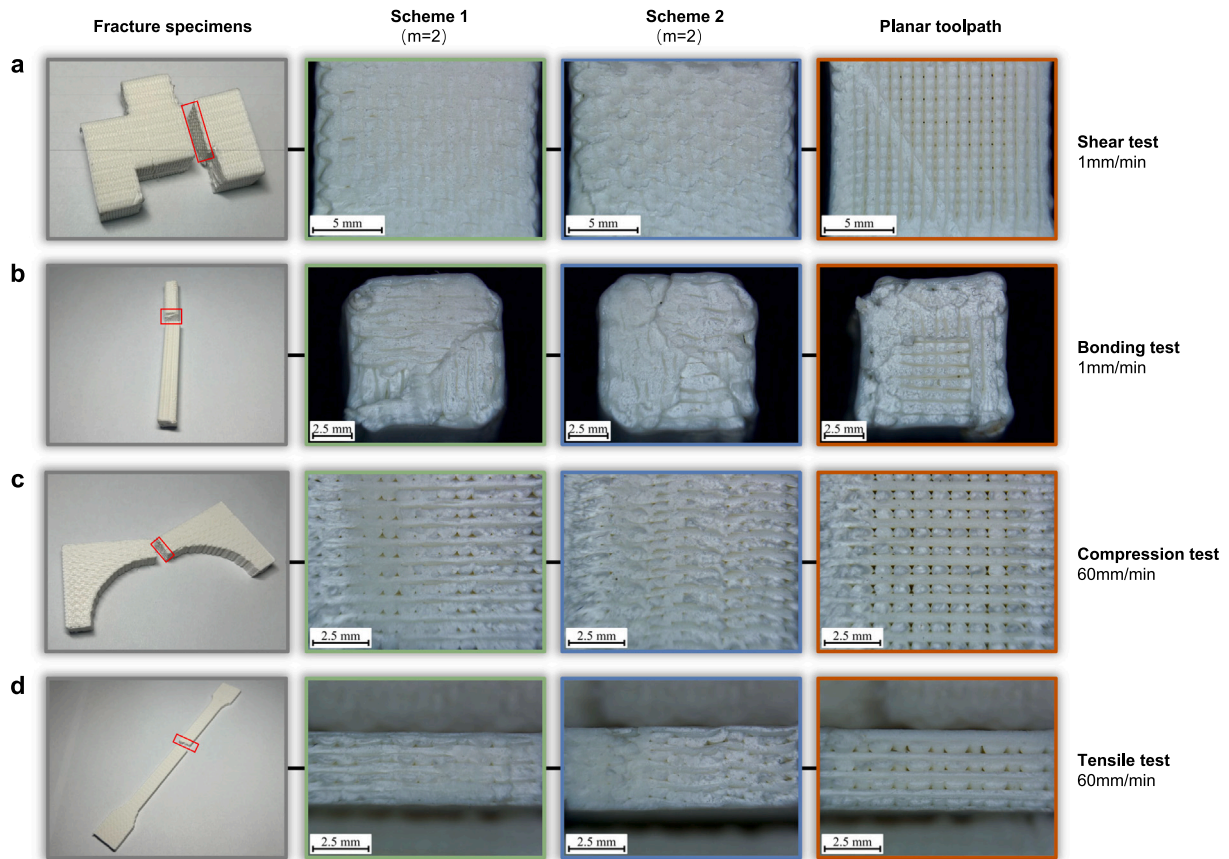


**Fig. 13. 3D video microscope images of the surfaces of the four test pieces after fracture. a** The Shear test at 1 mm/min. **b** The Bonding test at 1 mm/min. **c** The compression test at 60 mm/min. **d** The tensile test at 60 mm/min.

the toolpath between two layers. The two schemes we propose have undulating toolpaths up and down, and when the deposition head prints downward, it has the effect of "plowing", which produces extrusion on the toolpath of the lower layer. At the same time, the undulating toolpath has a larger contact area. In cross-section, our scheme shows a rougher surface, precisely because the layers are closer together. In contrast, the interlayer contact of the planar toolpath is not tight enough, and although the perimeter of the section has excess material that is extruded, resulting in good bonding around the perimeter, the overall bonding is not as strong as that of our proposed scheme.
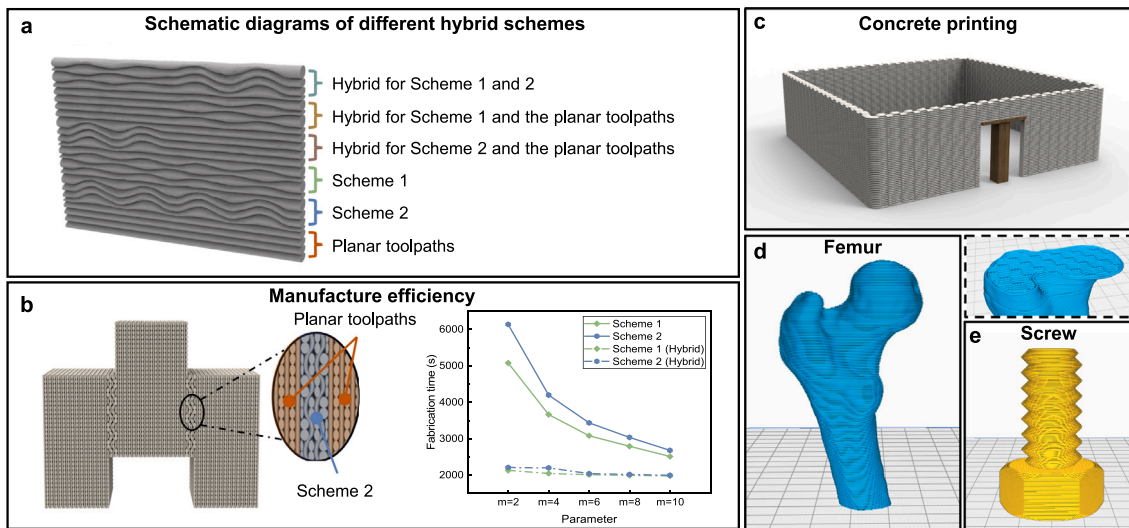
**Fig. 14. Application of hybrid toolpaths for different schemes. a** Schematic of our proposed hybrid toolpaths. **b** An example model. On the left, Scheme 2 is used for the high-shear stress region (see the zoomed-in blue region), and the planar toolpath method is used for the low-shear regions (see the zoomed-in orange region). On the right, the fabrication time curves are shown for different parameters *m*. **c** Application of our proposed method to concrete printing. **d** and **e** The toolpaths of the proposed schemes are utilized to blend with the out-of-plane contour toolpaths to achieve the fabrication of models with complex surfaces. (For interpretation of the references to color in this figure legend, the reader is referred to the web version of this article.)

In both compression and tension experiments, the fracture surfaces showed two main damage modes because the main load direction was vertical to the model construction direction. One is that the load direction is vertical to the toolpath direction, resulting in cracking between two adjacent toolpaths. This affects the performance of the specimen due to the relatively weak connection between the toolpaths. The other is that the load direction is parallel to the toolpath direction, when the structure of the toolpath itself is mainly damaged, and thus the fracture surface exhibits a rough character. All the specimens we used were printed in a layer-by-layer staggered manner. Therefore, from the fracture surface, it can be observed that half of the layers are cracked at the connection of neighboring toolpaths, and the other half of the layers are the destruction of the structure of the toolpath itself. However, as can be seen in Fig. 13a and b, the connection between the two neighboring toolpaths in our proposed scheme is much tighter, unlike the planar toolpath approach where gaps between the toolpaths. This advantage is attributed to the fact that the toolpaths have a "dumbbell" shape. As a result, it can be observed in Fig. 13c and d that the cracked section at the toolpath connection is rougher than the planar toolpath section in the layer where the toolpath direction is vertical to the loading direction, so more load is required to damage the specimen fabricated by our scheme.

## 4. Future perspectives

In this study, we designed two interlaced printing toolpath schemes for a conventional FFF 3-axis printer. Compared to the traditional planar toolpath method, these schemes not only have better in-plane mechanical properties but also greatly enhance interlayer shear resistance and bonding force. Compared to the non-planar toolpath methods in other studies, the proposed schemes are highly adaptable. For example, since they consist of numerous single toolpaths with periodic undulations. There can be many variants and infill structures with different infill densities for complex models of various sizes. Moreover, these schemes can effectively enhance the mechanical properties of the layers as shown in Section 3.2.

The interlaced printing toolpath method developed in this study can be further improved to degrade and selectively print models. For example, since the average thickness of each layer of the proposed schemes is $(h_{max} + h_{min})/2$, the different toolpath schemes can be used for different regions of the same model, as shown in Fig. 14a.

From bottom to top, the deposition toolpaths are the planar toolpaths, Scheme 2, Scheme 1, the hybrid for Scheme 2 and the planar toolpaths, the hybrid for Scheme 1 and the planar toolpaths, and the hybrid for Scheme 1 and 2, respectively. If further combined with the shear stress field after finite element analysis (FEA) or partitioning algorithms, the mechanical properties can be guaranteed while saving printing time, an example model is shown in Fig. 14b. Similarly, the use of external contours is crucial for aesthetic reasons. Our approach can generate external contours of a certain thickness on the outside and employ a planar toolpath approach at the first and last layers to enhance the surface accuracy of the model (see Fig. 14d and e).

Furthermore, we propose the method to make an intermittent undulating motion of the deposition head in the *Z*-axis direction at a specific position for each toolpath. Thus, it is not limited to a Zigzag-like toolpath in the infill structure, as demonstrated in this paper. It can also be Contour-like, Hilbert-like, Fermat spiral-like, and other toolpaths. Therefore, our proposed interlaced printing infill structure can be used as a complete or partial replacement for the conventional planar infill structure. It can be applied to many models, from high-precision models with thin-walled structures to large models with infill structures. Moreover, it can be integrated with concrete printing to enhance the mechanical properties of buildings (see Fig. 14c).

The proposed strategy has some limitations. For example, the *Z*-axis of most 3D printers uses a screw drive, which may reduce the molding efficiency of our method. In addition, the dynamically adjusted extrusion rate is subject to errors due to the delay in extruding the material by the printer. Although we minimized the loss by reducing the rated print speed, it was not fully resolved. If further improvements can be made to the hardware, such as trying to change the *Z*-axis of the printer to a synchronous belt drive or reducing the distance from the extrusion wheel to the extrusion head. In terms of algorithms, machine learning can be introduced to optimize the actual printing error [54,55]. These methods may be possible to better demonstrate the advantages of the proposed strategy.

## 5. Conclusion

In this paper, we present a nature-inspired interlaced printing strategy aimed at enhancing the mechanical properties of the model and demonstrating its effectiveness experimentally. First, the effect of the

strategy on the geometry of filaments is analyzed in depth at the microscopic level. Then, we compared it with conventional planar toolpaths in mechanical experiments, and the results showed that the method achieved significant results in improving the mechanical properties of the model, especially in the interlayer mechanical properties. We further analyzed the reasons for the improved mechanical properties of the method by observing the sample fracture in different experimental environments. In addition, since the geometries used in the study were formed by combinations of periodic toolpaths, the method applies to a wide range of features, including infill structures, outer walls, etc., and has the potential for a wide range of applications in a variety of fields, such as construction, biomedical, and industrial.

In future research, we plan to extend the method to other infill algorithms such as Contour [56], Fermat spiral [57], and even stress-based toolpath algorithms [49]. At the same time, we consider modifying the hardware or introducing machine learning techniques to reduce errors in the additive manufacturing process. This body of work will further advance the development of interlaced printing strategies to make them more comprehensive and innovative.

## CRediT authorship contribution statement

**Wenpeng Xu:** Writing – review & editing, Resources, Project administration, Funding acquisition. **Hao Xu:** Writing – original draft, Software, Methodology, Investigation, Formal analysis, Data curation. **Xiaoya Zhai:** Writing – review & editing, Resources, Formal analysis, Conceptualization. **Jingchao Jiang:** Writing – review & editing, Supervision, Resources, Project administration, Funding acquisition, Conceptualization.

## Declaration of competing interest

The authors declare that they have no known competing financial interests of personal relationships that could have appeared to influence the work reported in this paper.

## Data availability

The data supporting the findings of this study are available within the article.

## Acknowledgments

## Appendix A. Supplementary data

Supplementary material related to this article can be found online at https://doi.org/10.1016/j.addma.2024.104276.

• Movies S1 to S3

## References

[1] A. Uriondo, M. Esperon-Miguez, S. Perinpanayagam, The present and future of additive manufacturing in the aerospace sector: A review of important aspects, Proc. Inst. Mech. Eng. G 229 (11) (2015) 2132–2147, http://dx.doi.org/10.1177/0954410014568797.

[2] B. Blakey-Milner, P. Gradl, G. Snedden, M. Brooks, J. Pitot, E. Lopez, M. Leary, F. Berto, A. Du Plessis, Metal additive manufacturing in aerospace: A review, Mater. Des. 209 (2021) 110008, http://dx.doi.org/10.1016/j.matdes.2021.110008.

[3] R. Leal, F. Barreiros, L. Alves, F. Romeiro, J. Vasco, M. Santos, C. Marto, Additive manufacturing tooling for the automotive industry, Int. J. Adv. Manuf. Technol. 92 (2017) 1671–1676, http://dx.doi.org/10.1007/s00170-017-0239-8.

[4] J.C. Vasco, Additive manufacturing for the automotive industry, in: Additive Manufacturing, Elsevier, 2021, pp. 505–530, http://dx.doi.org/10.1016/B978-0-12-818411-0.00010-0.

[5] I. Valtonen, S. Rautio, M. Salmi, Capability development in hybrid organizations: Enhancing military logistics with additive manufacturing, Progress Addit. Manuf. 7 (5) (2022) 1037–1052, http://dx.doi.org/10.1007/s40964-022-00280-z.

[6] M. Javaid, A. Haleem, Additive manufacturing applications in medical cases: A literature based review, Alex. J. Med. 54 (4) (2018) 411–422, http://dx.doi.org/10.1016/j.ajme.2017.09.003.

[7] M. Salmi, Additive manufacturing processes in medical applications, Materials 14 (1) (2021) 191, http://dx.doi.org/10.3390/ma14010191.

[8] J. Jiang, X. Zhai, K. Zhang, L. Jin, Q. Lu, Z. Shen, W.-H. Liao, Low-melting-point alloys integrated extrusion additive manufacturing, Addit. Manuf. (2023) 103633, http://dx.doi.org/10.1016/j.addma.2023.103633.

[9] T. Rayna, L. Striukova, From rapid prototyping to home fabrication: How 3D printing is changing business model innovation, Technol. Forecast. Soc. Change 102 (2016) 214–224, http://dx.doi.org/10.1016/j.techfore.2015.07.023.

[10] Y. Zhao, J. Zhu, W. He, Y. Liu, X. Sang, R. Liu, 3D printing of unsupported multi-scale and large-span ceramic via near-infrared assisted direct ink writing, Nature Commun. 14 (1) (2023) 2381, http://dx.doi.org/10.1038/s41467-023-38082-8.

[11] M. Seleznev, J. Roy-Mayhew, J. Faust, Fabrication and tunable reinforcement of net-shaped aluminum matrix composite parts via 3D printing, Sci. Rep. 13 (1) (2023) 16334, http://dx.doi.org/10.1038/s41598-023-43514-y.

[12] W.C. Liu, V.H.Y. Chou, R.P. Behera, H. Le Ferrand, Magnetically assisted drop-on-demand 3D printing of microstructured multimaterial composites, Nat. Commun. 13 (1) (2022) 5015, http://dx.doi.org/10.1038/s41467-022-32792-1.

[13] D. Wangpraseurt, S. You, F. Azam, G. Jacucci, O. Gaidarenko, M. Hildebrand, M. Kühl, A.G. Smith, M.P. Davey, A. Smith, et al., Bionic 3D printed corals, Nat. Commun. 11 (1) (2020) 1748, http://dx.doi.org/10.1038/s41467-020-15486-4.

[14] Y. Liu, P. Zhang, H.-C. Zhang, W. Wang, T. Song, X. Yan, W. Zeng, Y.-J. Yang, Self-supporting parametric polyhedral structure for 3D printing, Adv. Eng. Softw. 186 (2023) 103529, http://dx.doi.org/10.1016/j.advengsoft.2023.103529.

[15] Z. Fang, C. Wu, C. Dai, Q. Shi, G. Fang, D. Xie, X. Zhao, Y.-J. Liu, C.C. Wang, X.-J. Wang, A multi-axis robot-based bioprinting system supporting natural cell function preservation and cardiac tissue fabrication, Bioactive Mater. 18 (2022) 138–150, http://dx.doi.org/10.1016/j.bioactmat.2022.02.009.

[16] Y. Sun, W. Tian, T. Zhang, P. Chen, M. Li, Strength and toughness enhancement in 3d printing via bioinspired tool path, Mater. Des. 185 (2020) 108239, http://dx.doi.org/10.1016/j.matdes.2019.108239.

[17] P.J. Tebon, B. Wang, A.L. Markowitz, A. Davarifar, B.L. Tsai, P. Krawczuk, A.E. Gonzalez, S. Sartini, G.F. Murray, H.T.L. Nguyen, et al., Drug screening at single-organoid resolution via bioprinting and interferometry, Nature Commun. 14 (1) (2023) 3168, http://dx.doi.org/10.1038/s41467-023-38832-8.

[18] B.N. Turner, R. Strong, S.A. Gold, A review of melt extrusion additive manufacturing processes: I. Process design and modeling, Rapid Prototyp. J. 20 (3) (2014) 192–204, http://dx.doi.org/10.1108/RPJ-01-2013-0012.

[19] J.F. Rodríguez, J.P. Thomas, J.E. Renaud, Mechanical behavior of acrylonitrile butadiene styrene fused deposition materials modeling, Rapid Prototyp. J. 9 (4) (2003) 219–230, http://dx.doi.org/10.1108/13552540310489604.

[20] Q. Sun, G. Rizvi, C. Bellehumeur, P. Gu, Effect of processing conditions on the bonding quality of FDM polymer filaments, Rapid Prototyp. J. 14 (2) (2008) 72–80, http://dx.doi.org/10.1108/13552540810862028.

[21] S.C. Partain, et al., Fused Deposition Modeling with Localized Pre-Deposition Heating Using Forced Air (Ph.D. thesis), Montana State University-Bozeman, College of Engineering, 2007.

[22] A.K. Ravi, A. Deshpande, K.H. Hsu, An in-process laser localized pre-deposition heating approach to inter-layer bond strengthening in extrusion based polymer additive manufacturing, J. Manuf. Process. 24 (2016) 179–185, http://dx.doi.org/10.1016/j.jmapro.2016.08.007.

[23] V. Kishore, C. Ajinjeru, A. Nycz, B. Post, J. Lindahl, V. Kunc, C. Duty, Infrared preheating to improve interlayer strength of big area additive manufacturing (BAAM) components, Addit. Manuf. 14 (2017) 7–12, http://dx.doi.org/10.1016/j.addma.2016.11.008.

[24] S. Shaffer, K. Yang, J. Vargas, M.A. Di Prima, W. Voit, On reducing anisotropy in 3D printed polymers via ionizing radiation, Polymer 55 (23) (2014) 5969–5979, http://dx.doi.org/10.1016/j.polymer.2014.07.054.

[25] C.B. Sweeney, B.A. Lackey, M.J. Pospisil, T.C. Achee, V.K. Hicks, A.G. Moran, B.R. Teipel, M.A. Saed, M.J. Green, Welding of 3D-printed carbon nanotube–polymer composites by locally induced microwave heating, Sci. Adv. 3 (6) (2017) e1700262, http://dx.doi.org/10.1126/sciadv.1700262.

[26] C. Duty, J. Failla, S. Kim, T. Smith, J. Lindahl, V. Kunc, Z-pinning approach for 3D printing mechanically isotropic materials, Addit. Manuf. 27 (2019) 175–184, http://dx.doi.org/10.1016/j.addma.2019.03.007.

[27] J. Jiang, S.T. Newman, R.Y. Zhong, A review of multiple degrees of freedom for additive manufacturing machines, Int. J. Comput. Integr. Manuf. 34 (2) (2021) 195–211, http://dx.doi.org/10.1080/0951192X.2020.1858510.

[28] G. Fang, T. Zhang, S. Zhong, X. Chen, Z. Zhong, C.C. Wang, Reinforced FDM: Multi-axis filament alignment with controlled anisotropic strength, ACM Trans. Graph. 39 (6) (2020) 1–15, http://dx.doi.org/10.1145/3414685.3417834.

[29] J. Etienne, N. Ray, D. Panozzo, S. Hornus, C.C. Wang, J. Martínez, S. McMains, M. Alexa, B. Wyvill, S. Lefebvre, CurviSlicer: Slightly curved slicing for 3-axis printers, ACM Trans. Graph. 38 (4) (2019) 1–11, http://dx.doi.org/10.1145/3306346.3323022.

[30] D. Chakraborty, B.A. Reddy, A.R. Choudhury, Extruder path generation for curved layer fused deposition modeling, Comput. Aided Des. 40 (2) (2008) 235–243, http://dx.doi.org/10.1016/j.cad.2007.10.014.

[31] B. Huang, S.B. Singamneni, Curved layer adaptive slicing (CLAS) for fused deposition modelling, Rapid Prototyp. J. 21 (4) (2015) 354–367, http://dx.doi.org/10.1108/RPJ-06-2013-0059.

[32] Y. Jin, J. Du, Y. He, G. Fu, Modeling and process planning for curved layer fused deposition, Int. J. Adv. Manuf. Technol. 91 (2017) 273–285, http://dx.doi.org/10.1007/s00170-016-9743-5.

[33] B. Ezair, S. Fuhrmann, G. Elber, Volumetric covering print-paths for additive manufacturing of 3D models, Comput. Aided Des. 100 (2018) 1–13, http://dx.doi.org/10.1016/j.cad.2018.02.006.

[34] L. Pelzer, C. Hopmann, Additive manufacturing of non-planar layers with variable layer height, Addit. Manuf. 37 (2021) 101697, http://dx.doi.org/10.1016/j.addma.2020.101697.

[35] P. Schaechtl, B. Schleich, S. Wartzack, On the potential of slicing algorithms in additive manufacturing for the optimization of geometrical part accuracy, Procedia CIRP 114 (2022) 215–220, http://dx.doi.org/10.1016/j.procir.2022.10.030.

[36] H.-m. Zhao, Y. He, J.-z. Fu, J.-j. Qiu, Inclined layer printing for fused deposition modeling without assisted supporting structure, Robot. Comput.-Integr. Manuf. 51 (2018) 1–13, http://dx.doi.org/10.1016/j.rcim.2017.11.011.

[37] Y. Yao, C. Ding, M. Aburaia, M. Lackner, L. He, A 3D weaving infill pattern for fused filament fabrication, Int. J. Adv. Manuf. Technol. 117 (9–10) (2021) 3101–3114, http://dx.doi.org/10.1007/s00170-021-07694-z.

[38] J. Allum, J. Kitzinger, Y. Li, V.V. Silberschmidt, A. Gleadall, ZigZagZ: Improving mechanical performance in extrusion additive manufacturing by nonplanar toolpaths, Addit. Manuf. 38 (2021) 101715, http://dx.doi.org/10.1016/j.addma.2020.101715.

[39] H.K. Raut, A.F. Schwartzman, R. Das, F. Liu, L. Wang, C.A. Ross, J.G. Fernandez, Tough and strong: Cross-lamella design imparts multifunctionality to biomimetic nacre, ACS Nano 14 (8) (2020) 9771–9779, http://dx.doi.org/10.1021/acsnano.0c01511.

[40] J. Rivera, M.S. Hosseini, D. Restrepo, S. Murata, D. Vasile, D.Y. Parkinson, H.S. Barnard, A. Arakaki, P. Zavattieri, D. Kisailus, Toughening mechanisms of the elytra of the diabolical ironclad beetle, Nature 586 (7830) (2020) 543–548, http://dx.doi.org/10.1038/s41586-020-2813-8.

[41] M.A. Meyers, J. McKittrick, P.-Y. Chen, Structural biological materials: Critical mechanics-materials connections, Science 339 (6121) (2013) 773–779, http://dx.doi.org/10.1126/science.1220854.

[42] U.G. Wegst, H. Bai, E. Saiz, A.P. Tomsia, R.O. Ritchie, Bioinspired structural materials, Nat. Mater. 14 (1) (2015) 23–36, http://dx.doi.org/10.1038/nmat4089.

[43] X. Li, W.-C. Chang, Y.J. Chao, R. Wang, M. Chang, Nanoscale structural and mechanical characterization of a natural nanocomposite material: The shell of red abalone, Nano Lett. 4 (4) (2004) 613–617, http://dx.doi.org/10.1021/nl049962k.

[44] X. Li, Z.-H. Xu, R. Wang, In situ observation of nanograin rotation and deformation in nacre, Nano Lett. 6 (10) (2006) 2301–2304, http://dx.doi.org/10.1021/nl061775u.

[45] J. Rivera, S. Murata, M.S. Hosseini, A.A. Trikanad, R. James, A. Pickle, N. Yaraghi, N. Matsumoto, W. Yang, D.Y. Parkinson, et al., Structural design variations in beetle elytra, Adv. Funct. Mater. 31 (50) (2021) 2106468, http://dx.doi.org/10.1002/adfm.202106468.

[46] Y.A. Shin, S. Yin, X. Li, S. Lee, S. Moon, J. Jeong, M. Kwon, S.J. Yoo, Y.-M. Kim, T. Zhang, et al., Nanotwin-governed toughening mechanism in hierarchically structured biological materials, Nat. Commun. 7 (1) (2016) 10772, http://dx.doi.org/10.1038/ncomms10772.

[47] L. Li, C. Ortiz, A natural 3D interconnected laminated composite with enhanced damage resistance, Adv. Funct. Mater. 25 (23) (2015) 3463–3471, http://dx.doi.org/10.1002/adfm.201500380.

[48] Z.H. Aitken, S. Luo, S.N. Reynolds, C. Thaulow, J.R. Greer, Microstructure provides insights into evolutionary design and resilience of Coscinodiscus sp. frustule, Proc. Natl. Acad. Sci. 113 (8) (2016) 2017–2022, http://dx.doi.org/10.1073/pnas.1519790113.

[49] W. Xu, H. Xu, Q. Li, P. Zhang, L. Yang, W. Wang, Stress-based continuous planar path planning for additive manufacturing, Adv. Eng. Softw. (2024) 103544, http://dx.doi.org/10.1016/j.advengsoft.2023.103544.

[50] W. Xu, Q. Li, H. Xu, X. Zhai, J. Jiang, Voxel-based variable width continuous spiral path planning for 3D printing, J. Manuf. Process. 107 (2023) 226–239, http://dx.doi.org/10.1016/j.jmapro.2023.10.044.

[51] F. Zhong, Y. Xu, H. Zhao, L. Lu, As-continuous-as-possible extrusion-based fabrication of surface models, ACM Trans. Graph. 42 (3) (2023) 1–16, http://dx.doi.org/10.1145/3575859.

[52] Clipper, ClipperLib. http://www.angusj.com/delphi/clipper/documentation/Docs/Units/ClipperLib/_Body.htm.

[53] A. Moetazedian, A.S. Budisuharto, V.V. Silberschmidt, A. Gleadall, CONVEX (continuously varied extrusion): A new scale of design for additive manufacturing, Addit. Manuf. 37 (2021) 101576, http://dx.doi.org/10.1016/j.addma.2020.101576.

[54] J. Jiang, A survey of machine learning in additive manufacturing technologies, Int. J. Comput. Integr. Manuf. 36 (9) (2023) 1258–1280, http://dx.doi.org/10.1080/0951192X.2023.2177740.

[55] T.S. Tamir, G. Xiong, Q. Fang, Y. Yang, Z. Shen, M. Zhou, J. Jiang, Machine-learning-based monitoring and optimization of processing parameters in 3D printing, Int. J. Comput. Integr. Manuf. 36 (9) (2023) 1362–1378, http://dx.doi.org/10.1080/0951192X.2022.2145019.

[56] Y. Yang, H.T. Loh, J. Fuh, Y. Wang, Equidistant path generation for improving scanning efficiency in layered manufacturing, Rapid Prototyp. J. 8 (1) (2002) 30–37, http://dx.doi.org/10.1108/13552540210413284.

[57] H. Zhao, F. Gu, Q.-X. Huang, J. Garcia, Y. Chen, C. Tu, B. Benes, H. Zhang, D. Cohen-Or, B. Chen, Connected fermat spirals for layered fabrication, ACM Trans. Graph. 35 (4) (2016) 1–10, http://dx.doi.org/10.1145/2897824.2925958.